

pubs.acs.org/EF Article

Carbon Foam/CaCl₂·6H₂O Composite as a Phase-Change Material for Thermal Energy Storage

Yikang Jing, Kunal Dixit, Scott N. Schiffres, and Hao Liu*



Cite This: Energy Fuels 2023, 37, 12381-12390



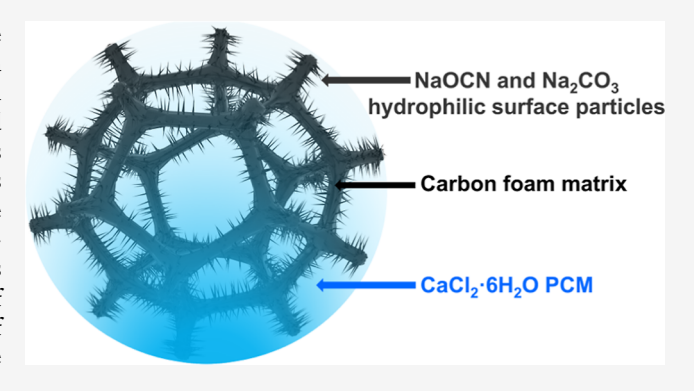
ACCESS

III Metrics & More

Article Recommendations

Supporting Information

ABSTRACT: Inorganic salt hydrates are promising phase-change materials (PCMs) for thermal energy storage due to their high latent heat of fusion. However, their practical application is often limited by their unstable form, dehydration, large supercooling, and low thermal conductivity. Porous melamine foam and its carbonized derivatives are potential supporting porous materials to encapsulate inorganic salt hydrate PCMs to address these problems. This work investigates the effect of pyrolysis temperature on the morphology and structure of the carbonized foams and their thermal energy storage performance. Pyrolysis of melamine foam at 700–900 °C leads to the formation of crystalline sodium cyanate and sodium carbonate particles on the foam skeleton surface, which allows the spontaneous impregnation



of the carbon foam with molten $CaCl_2 \cdot 6H_2O$. The form-stable foam- $CaCl_2 \cdot 6H_2O$ composite effectively suppresses supercooling and dehydration, demonstrating the efficacy of carbon foam as a promising supporting material for inorganic salt hydrate PCMs.

1. INTRODUCTION

Phase-change materials (PCMs) play an important role in thermal energy storage and temperature regulation. In a PCM, energy is stored as latent heat through a reversible phase change without temperature changes. Among a variety of PCMs, solid materials leveraging the solid-liquid phase change (solid-liquid PCMs) are promising candidates for energy storage in a wide range of applications, such as solar energy storage, temperature regulation in buildings, and electronics³ because of their high energy density and safety. Organic solid-liquid PCMs (e.g., paraffin wax) have been commercialized nowadays,4 yet they suffer from flammability and high cost. In contrast, inorganic solid-liquid PCMs are nonflammable and generally exhibit larger latent heat than their organic counterparts.5 For example, inorganic salt hydrates exhibit more than twice as much energy density as organic PCMs while maintaining a low cost of manufacturing. Nonetheless, the practical application of inorganic salt hydrates is undermined by large supercooling during recrystallization and phase separation induced by dehydration during heating. In addition, the solid form of the solid-liquid PCMs cannot be maintained upon melting, which also results in a precipitous drop in thermal conductivity.

Various strategies have been proposed to address these problems for inorganic salt hydrate PCMs. The addition of thickeners [e.g. carboxyl methylcellulose (CMC), gelatin, and polyacrylamide (PAM)] and nucleating agents [e.g. BaI₂· 6H₂O, BaCl₂, BaCO₃, and Sr(OH)₂] is effective in suppressing dehydration and supercooling, respectively.^{8,9} The strategy for

form-stable PCM invariably involves the adsorption and impregnation of PCMs into various porous materials, including porous carbon-based materials, porous mineral-based materials, metal foams, polymer foams, and silica matrices. $^{6,10-13}$ Recent studies on the intrinsic defects of salt hydrates have demonstrated suppressed dehydration and supercooling through the confinement of PCM in porous materials. 14,15 Of these, carbon-based porous materials are particularly promising because of their low cost, high thermal and chemical stability, and high thermal conductivity (0.01–2000 W m $^{-1}$ K $^{-1}$). $^{16-18}$

Carbonized melamine foam (CMF) presents a promising alternative as a host material for PCMs owing to its low density and high porosity. CMFs synthesized at different conditions have been used as supporting materials for various PCMs, such as paraffin wax, ¹⁹ polyethylene glycol, ²⁰ and Na₂S₂O₃·5H₂O-NaOAc·3H₂O. ²¹ However, their volumetric and gravimetric fraction limitation in the composite PCMs is not quantitatively demonstrated. Although the hydrophobic nature of the carbon surface seems to prohibit the impregnation of inorganic salt hydrates in CMF, previous studies on the pyrolysis of

Received: April 13, 2023 Revised: July 7, 2023 Published: July 26, 2023





melamine foam (MF) have demonstrated a change to hydrophilic behavior at high pyrolysis temperature (>700 °C).²² Thus, tuning the pyrolysis temperature is a viable option to enable the inorganic salt hydrate composite PCMs.

Here, we adopt CaCl₂·6H₂O as the inorganic salt hydrate PCM to study the effect of the pyrolysis temperature of CMF on the thermal storage properties and performance of the CMF-CaCl₂·6H₂O composite. CaCl₂·6H₂O is an important salt hydrate PCM for temperature regulation due to its low melting point (28.4 °C),²³ high heat of fusion (185.6 J/g),²³ and low cost. However, like many other inorganic salt hydrate PCMs, pure CaCl₂·6H₂O suffers from large supercooling, substantial dehydration, and limited thermal conductivity. Porous media, such as diatomite, 23 expanded perlite, 24 and expanded graphite, 25 have been used to encapsulate CaCl₂· 6H₂O to address these problems. Encapsulation of CaCl₂· 6H₂O in diatomite reduces the supercooling of CaCl₂·6H₂O by ~10 °C and increases the onset temperature for dehydration.²³ The porous host material also modifies the thermal conductivity of the composite. For example, heat passing through the CaCl₂·6H₂O is impeded by the low thermal conductivity expanded perlite domains,²⁴ while an increase is observed for impregnation in expanded graphite.²⁵ Although these porous materials are effective in maintaining the form of CaCl₂·6H₂O after melting, the high weight fraction of the porous material (e.g., 10-50 wt % for expanded graphite; 40 wt % diatomite or expanded perlite) undermines the energy density for practical applications. To increase the energy density of the composite PCM, it is necessary to reduce the weight and volume fraction of the porous host material.

In this work, we studied the effect of the MF pyrolysis temperature on the wetting and thermal properties of the composite CaCl₂·6H₂O PCM. High pyrolysis temperature imparts hydrophilicity to the CMF that allows nearly full impregnation of the molten CaCl₂·6H₂O. The origin of the hydrophilic property was investigated by a combination of scanning electron microscopy (SEM), Fourier-transform infrared spectroscopy (FTIR), and powder X-ray diffraction (XRD) studies, which reveal substantial changes in the physical and chemical properties of CMF as a function of the pyrolysis temperature. The use of carbon foam suppresses the leakage, supercooling, and dehydration of CaCl₂·6H₂O. This study demonstrates CMF as a promising host material for inorganic salt hydrate PCMs.

2. MATERIALS AND EXPERIMENTS

- **2.1. Materials.** Calcium chloride hexahydrate ($CaCl_2 \cdot 6H_2O$, 99%) was purchased from Sigma-Aldrich. MF was obtained from Oh My Clean Co., Ltd.
- **2.2. Sample Preparation.** *2.2.1. Preparation of CMF.* The synthesis of CMF followed the same procedure as previously reported by Hou et al.²⁶ The MF was cut into 1 cm × 4.4 cm × 26 cm blocks, which were then loaded in an STF1200 tube furnace (Across International). The carbonization of the MF was performed at 400 °C, 600 °C, 800 °C, or 1000 °C for 60 min under flowing argon at a 3 °C/min heating ramp. These CMF samples are denoted as CMF400, CMF600, CMF800, and CMF1000, respectively. CMFs were cut with a hole punch into cylinders of 18 mm diameter for subsequent experiments and characterization.
- 2.2.2. Preparation of CaCl₂·6H₂O/MF and CaCl₂·6H₂O/CMF Composite PCM (Three Methods). CaCl₂·6H₂O (10 g) was first fully melted in identically sealed 27 mm × 55 mm (diameter × height) glass vials placed into a water bath at 40 °C. Three impregnation methods were used to infiltrate the foams with the salt

hydrate: soaking, squeezing, and vacuum impregnation (Figures 1 and S1).

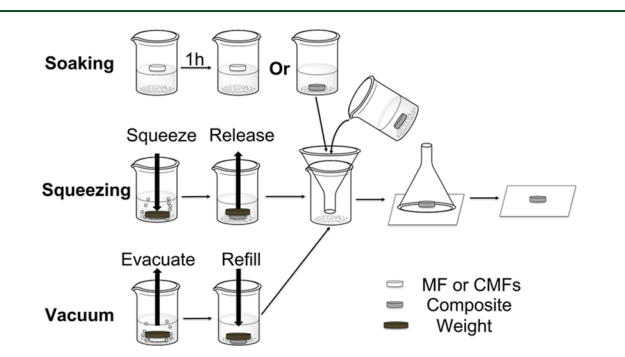


Figure 1. Schematic illustration of the soaking, squeezing, and vacuum impregnation methods to impregnate MF and CMFs with molten $CaCl_2 \cdot 6H_2O$.

- 2.2.2.1. Soaking Impregnation. MF and CMFs were directly loaded into the vials on top of the molten salt. The sealed vials were kept in a water bath at 40 $^{\circ}$ C for 1 h.
- 2.2.2.2. Squeezing Impregnation. MF or CMFs were first compressed by a weight in molten $CaCl_2 \cdot 6H_2O$ to expel the air trapped inside the foams. Once the pressure was released, the foams were restored to their original form concurrent with the impregnation with molten $CaCl_2 \cdot 6H_2O$.
- 2.2.2.3. Vacuum Impregnation. MF or CMFs were first introduced into molten $CaCl_2 \cdot 6H_2O$ and kept submerged by a weight. The vials were then evacuated to expel the air trapped in the foams. Molten $CaCl_2 \cdot 6H_2O$ was impregnated into the foams when the vial was refilled to ambient pressure.

The impregnated foams were filtered out by a Buchner funnel and transferred to a polytetrafluoroethylene sheet before being frozen in the fridge at $-17\,^{\circ}\text{C}.$ SMF, SCMF400, SCMF600, SCMF800, and SCMF1000 are used to denote the salt hydrate composites obtained by the impregnation of MF, CMF400, CMF600, CMF800, and CMF1000 with CaCl $_2$ -6H $_2$ O, respectively.

- **2.3. Sample Characterization.** *2.3.1. Porosity Characterization.* The open pore volume per unit mass of the foams was measured by the imbibition method²⁷ using dimethyl sulfoxide (DMSO, ≥99.9%, density: 1.10 g/mL, Honeywell) as the solvent. The foam was soaked with DMSO, and the open pore volume was determined by the volume of the impregnated DMSO. The density of the foam skeleton excluding open voids was measured by a 1200E micro-ultrapycnometer (Quantachrome Instrument Inc., USA).
- 2.3.2. Scanning Electron Microscopy (SEM). SEM (Supra 55VP, Zeiss) operating with an accelerating voltage of 1–10 kV was used to characterize the foam morphology.
- 2.3.3. Fourier-Transform Infrared (FTIR) Spectroscopy. Foams were ground into powder in a mortar and pestle for the characterization of the functional groups by a FTIR spectrometer (Nicolet 8700, Thermo Electron Inc., USA) with a wavelength range between 650 and 4000 cm⁻¹ in the attenuated total reflection mode.
- 2.3.4. X-ray Powder Diffraction (XRD). Crushed foam powder was measured by a powder X-ray diffractometer (Bruker D8 ADVANCE X-ray diffractometer) in Bragg—Brentano geometry at room temperature with Mo K α radiation between 5 and 55° 2 θ .
- 2.3.5. Thermogravimetric Analysis (TGA). Dehydration of pure CaCl $_2$ ·6H $_2$ O and its composites was measured by a TGA analyzer (Q50, TA Instrument Inc., USA) with 1 $^{\circ}$ C/min heating ramp from room temperature to 60 $^{\circ}$ C.
- 2.3.6. Differential Scanning Calorimetry (DSC). The phase-change temperatures and phase-change enthalpies were measured by a DSC calorimeter (Q200, TA Instrument Inc., USA) in the range of -40 to 60 °C with a ramp rate of 10 °C/min under nitrogen atmosphere (50 mL/min). The accuracy of the temperature measurement was within ± 0.1 °C and that of the calorimeter was within ± 0.1 %. Samples were

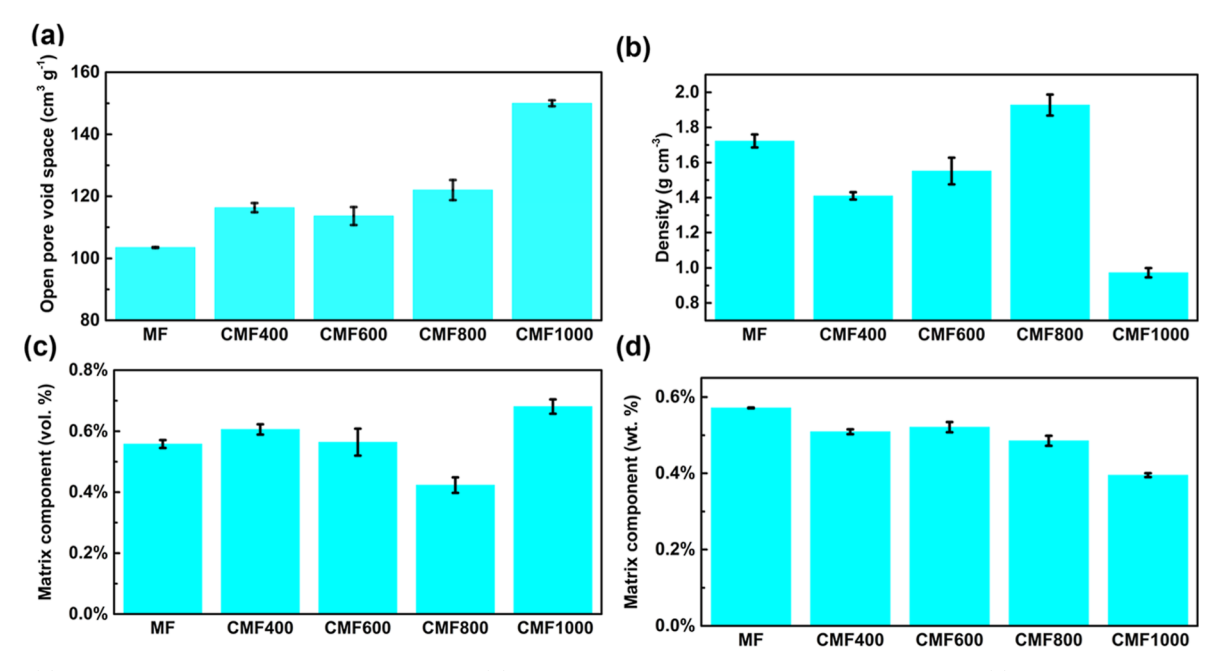


Figure 2. (a) Open pore space per unit mass of the foams; (b) density of the solid skeleton excluding open voids; (c) calculated matrix component (vol %) of the foam in the $CaCl_2 \cdot 6H_2O/MF$ (carbon foam) composite; and (d) calculated matrix component (wt %) of the foam in the $CaCl_2 \cdot 6H_2O/MF$ (carbon foam) composite.

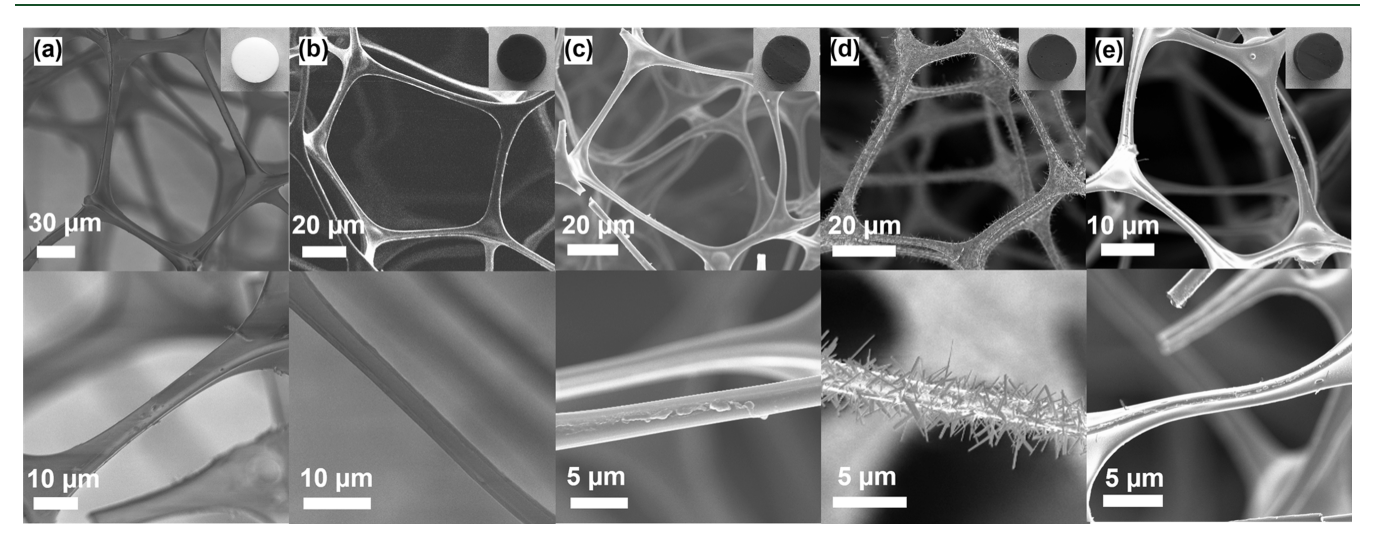


Figure 3. SEM images of (a) MF, (b) CMF400, (c) CMF600, (d) CMF800, and (e) CMF1000. Inset shows the photograph of the foam pellet.

measured in aluminum Tzero Pans with a Tzero Hermetic Lid. The loading mass of samples was \sim 15 mg.

2.3.7. Thermal Conductivity. The thermal conductivity of molten CaCl₂·6H₂O and molten CaCl₂·6H₂O/MF(CMFs) composites was measured by the transient hot wire method, ²⁸ which used a 25 μ m diameter platinum wire with a 5 μ m thick polyethylene terephthalate insulation layer (Goodfellow, USA) and a 200 μ m penetration depth.

2.3.8. 3D X-ray CT Scanning. The 3D X-ray CT images of the solid CaCl₂·6H₂O/MF composite were acquired at a resolution of 3 μ m per voxel by an X-ray inspection system (Phoenix Nanomelx X-ray inspection system).

3. RESULTS AND DISCUSSION

3.1. Characterization of MF and CMF. 3.1.1. Density and Open Porosity. To determine the mass and volume fraction of the foam skeleton in the carbon foam composite, we measured the open space of the carbon foam blocks (Figure 2a) and the density of the solid foam skeleton (Figure 2b). The

calculated volume fraction (open porosity) and mass fraction of foams in the CaCl₂·6H₂O composite PCM are shown in Figure 2c,d, respectively. The open space for the MF is 103.5 \pm 0.2 cm³/g and increases with pyrolysis temperature from $116.3 \pm 1.5 \text{ cm}^3/\text{g}$ for CMF400 to $150 \pm 1 \text{ cm}^3/\text{g}$ for CMF1000. The measured density of the skeleton component of MF is $1.72 \pm 0.04~\mathrm{g~cm^{-3}}$, which corresponds to an apparent density (defined as the total mass divided by the geometric volume, including porosity) of 9.6 mg cm⁻³. This value is well within the range of the apparent density (4-12 mg cm⁻³) reported for MF.²⁶ After carbonization at 400 °C for 1 h, the solid component's density decreases to $1.41 \pm 0.02 \text{ g/cm}^3$, which is consistent with the previous report for carbonized MF.²² The density of the solid component of the CMF increases with the pyrolysis temperature to $1.92 \pm 0.06 \text{ g/cm}^3$ for CMF800. This density increase suggests the formation of sp² carbon clusters with increasing temperature.²⁹ However,

Energy & Fuels pubs.acs.org/EF Article

the density decreases to 0.97 ± 0.03 g/cm³ for the CMF1000, which is ascribed to the formation of closed pores inside the carbon skeleton (Figure S2). By comparison, the density of graphite is 2.26 g/cm³.³⁰ For all MF and CMFs, the volumetric and gravimetric fraction of the foam in the CaCl₂·6H₂O composite is less than 1% (Table S1).

3.1.2. Microstructure. The microstructure of MF and CMFs was examined by SEM (Figures 3 and S4). The skeleton structure of MF is maintained for all foams after pyrolysis. The average skeleton length decreases with increasing pyrolysis temperature until 600 °C and remains effectively constant from 600 to 1000 °C (Figure S3). Substantial changes in the morphology of the skeleton surface are observed for different pyrolysis temperatures: smooth surface is observed for pyrolysis temperatures up to 600 °C and at 1000 °C, but a layer of thorn-like particle deposits is observed for CMF800 (Figure 3). These surface deposits start to appear on the surface as spherical particles at 700 °C, evolving into spikes at 800 °C, and mostly disappear around 900 °C (Figure S4a). The morphology of the surface deposits is also affected by the pyrolysis duration: the spikes observed for 1 h pyrolysis at 800 °C evolve into ellipsoidal shape for 6 h pyrolysis at 800 °C and degrade substantially into nanoparticles for 24 h pyrolysis at 800 °C (Figure S4b). Similar surface deposits have been observed in the literature for the pyrolysis of MF at temperatures higher than 600 °C and are attributed to sodium carbonate. 22 Sodium and oxygen are from the blowing agent and formaldehyde during MF production, respectively.

3.1.3. XRD. To characterize the crystallinity and to interrogate the nature of the surface particles in CMF800, powder XRD was performed for crushed samples of MF and CMFs (Figures 4 and S5). No Bragg peak is observed for MF,

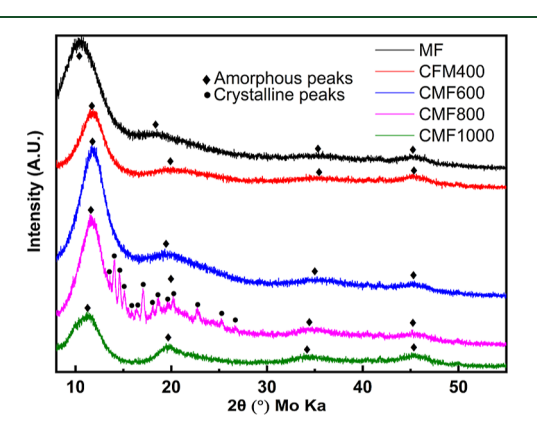


Figure 4. X-ray powder diffraction patterns of the MF and CMFs pyrolyzed at 400 °C (CMF400), 600 °C (CMF600), 800 °C (CMF800), and 1000 °C (CMF1000). Bragg peaks are observed for CMF800 due to the generated crystalline surface particles of Na_2CO_3 , $Na_2CO_3 \cdot H_2O$, and NaOCN.

CMF400, CMF600, or CMF1000, demonstrating the amorphous nature of these samples. However, Bragg peaks are observed for samples pyrolyzed at 700, 800, and 900 °C (Figure S5), which corresponds to the formation of crystalline components in the pyrolyzed samples. Most Bragg peaks can be explained by sodium carbonate $(Na_2CO_3)^{31}$ and sodium carbonate monohydrate $(Na_2CO_3\cdot H_2O)^{32}$ as suggested by the previous C 1s X-ray photoelectron spectroscopy study of carbonized MF. The hydrated phase is likely the result of exposing the samples to air before the XRD measurement.

However, the carbonate phases cannot explain the prominent peak at 14° observed for CMF700 and CMF800. A thorough search of potential phases suggests sodium cyanate (NaOCN)^{33,34} as the most plausible phase to explain this Bragg peak. It is noted that the synthesis of NaOCN from sodium carbonate and urea takes place at 525–650 °C,³⁵ which is close to the pyrolysis temperature for CMF700 and CMF800. This cyanate phase disappears when the pyrolysis temperature is above 800 °C, which is evident in the disappearance of the Bragg peaks for NaOCN for CMF900. Good profile fitting can be obtained when the cyanate phase is included in the Rietveld refinement for CMF700 and CMF800 (only the lattice parameters are refined without the refinement of the structural parameters) (Figures 5 and S6). The refined

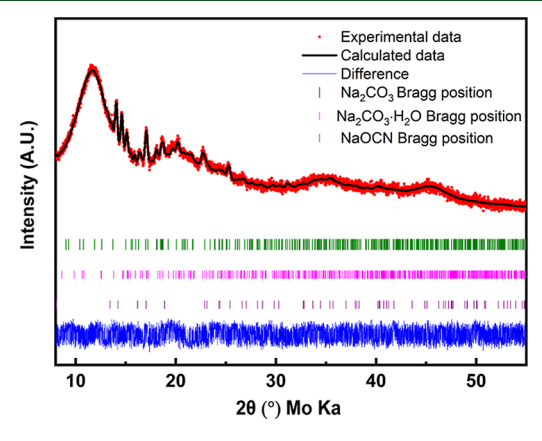


Figure 5. Observed and calculated (Rietveld method) X-ray powder diffraction pattern for the CMF pyrolyzed at 800 $^{\circ}$ C (CMF800). The Rietveld refined relative weight fractions of Na₂CO₃ Na₂CO₃·H₂O, and NaOCN are 16.32, 60.46, and 23.23 wt %, respectively.

domain size for the carbonate and cyanate phases is \sim 30 nm, which is similar to the particle size of the surface deposits observed for CMF700, CMF800, and CMF900 samples. This is consistent with the assignment of the surface deposits to the sodium carbonate and cyanate species and the concurrent observation of Bragg peaks and surface deposits.

No crystalline carbon phase is observed up to 1000 $^{\circ}$ C pyrolysis. Previous work on the pyrolysis of melamine to prepare graphitic carbon nitride (g-C₃N₄) requires repeated annealing at elevated temperatures (e.g., 800 $^{\circ}$ C), 36 which explains the lack of crystalline carbon phases in the CMF samples.

3.1.4. FTIR Spectroscopy. The evolution of the functional groups of the foams with the pyrolysis temperature was characterized by FTIR (Figures 6 and S7). The FTIR spectrum for MF is consistent with the previous study, ²² where peaks at 812 and 1550 cm⁻¹ are assigned to the bending mode and C=N stretching of the triazine ring, respectively. The weak peaks observed at 2930 and 3370 cm⁻¹ are assigned to C-H stretching and N-H stretching, respectively. ^{22,37-39} The peaks at 1480 and 1170 cm⁻¹ are assigned to the bending mode of the methylene C-H and the stretching mode of C-O, respectively. ^{37,39} The peak at 1340 cm⁻¹ should originate from the stretching mode of C-N, the carbon atom of which is part of the s-triazine ring. ^{40,41} The peak at 1020 cm⁻¹ can be assigned to ring deformation vibrations. ⁴² Pyrolysis up to 600 °C results in the disappearance of the peaks associated with the triazine rings, indicating the decomposition of the triazine ring. Meanwhile, the C-N stretching peak becomes a broad band

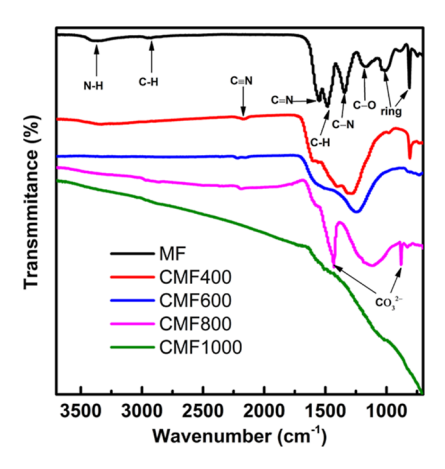


Figure 6. FTIR spectra of MF and CMFs pyrolyzed at 400 °C (CMF400), 600 °C (CMF600), 800 °C (CMF800), and 1000 °C (CMF1000).

and gradually shifts from 1340 to 1120 cm⁻¹ along with the increase of pyrolysis temperature. This should be because the aromatic triazine ring containing the carbon atom of C-N is broken down into aliphatic compounds, 40,41 and the C-N and C-O stretching peaks overlap with each other. Two peaks at 2150 and 2220 cm⁻¹ appear at 400 °C. These two peaks have been previously assigned to the stretching of C≡N or C≡ C. 22,38 However, they are also consistent with the assignment to the cyanate group in NaOCN. 43 These peaks first appear at 400 °C and persist until 800 °C, which agrees well with the observation of NaOCN in the XRD patterns. When the pyrolysis temperature reaches 800 °C, a sharp peak at 881 cm⁻¹ and a broad peak at 1430 cm⁻¹ are observed, both of which are characteristic of carbonate groups in Na₂CO₃. ⁴⁴ The carbonate peaks disappear when the pyrolysis temperature is above 1000 °C. This assignment is consistent with the observation of the carbonate phases in the XRD. For CMF1000, no obvious peaks are observed, which indicates the elimination of functional groups in the raw MF.

3.2. Wettability of MF and CMFs with Water and CaCl₂·6H₂O. The water impregnation efficiency (defined as the volume fraction of the open void space occupied by the liquid phase, eq S1) by the soaking method is used as a proxy for the hydrophilicity of the MF and CMFs (Figure S9). Except for CMF1000, all MF and CMFs readily soak up water with high efficiency (>96%).

Notwithstanding the observed hydrophilicity of MF and CMF400, CMF600, and CMF800, not all foams readily wet the molten $CaCl_{2}\cdot 6H_{2}O$ (Figures 7 and S8). The $CaCl_{2}\cdot 6H_{2}O$ impregnation efficiency by the soaking method is used as a proxy for the wettability of the MF and CMFs with CaCl₂. 6H₂O. The impregnation efficiencies of CMF700, CMF800, and CMF900 are 94.23%, 97.23%, and 93.15%, respectively, whereas those of MF, CMF400, CMF600, and CMF1000 are 0.19%, 0.09%, 0.15%, and 0.01% respectively. This shows that CMF700, CMF800, and CMF900 readily wet molten CaCl₂· 6H₂O, while other foams do not. The wettability with the salt hydrate correlates with the formation of surface deposits of hydrophilic sodium carbonates and cyanate. This observation is consistent with the reported hydrophilic property of the MF pyrolyzed at 800 °C.²² The surface sodium deposits have been shown to impart the hydrophilicity of the carbonized foam, which also explains the wetting result in the present work. It is remarkable that hydrophilicity as measured by water

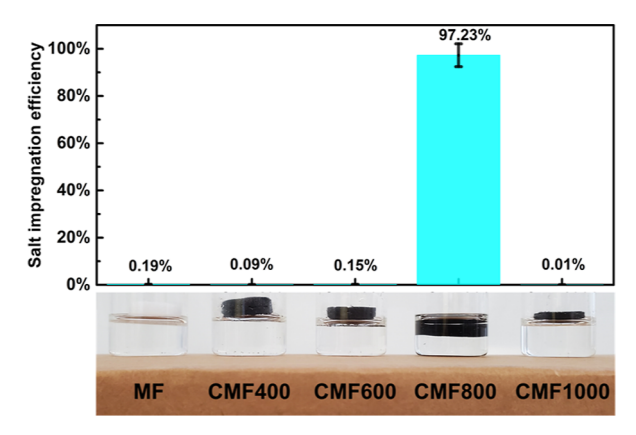


Figure 7. Impregnation efficiency of the foams using soaking impregnation (top panel) and photographs of the foams and the molten CaCl₂·6H₂O after the soaking impregnation (bottom panel).

impregnation efficiency does not correlate with the wettability of the foam with the molten $CaCl_2 \cdot 6H_2O$. This lack of correlation is attributed to the increased surface tension of the salt hydrate that cannot wet a weakly hydrophilic surface. ⁴⁵

3.3. Impregnation Efficiency of Different Impregnation Methods. In the absence of spontaneous impregnation in samples other than CMF800, squeezing and vacuum impregnation methods were used to introduce molten salt in the porous space (Figures 1 and S1). Both methods utilize a pressure difference between the porous interior of the foam and the molten salt solution to overcome the interfacial energy of a nonwetting surface during molten salt impregnation.

For the squeezing impregnation method, the salt impregnation efficiency of MF and CMFs decreases with increasing pyrolysis temperature (Figure 8). In contrast, the impregnation

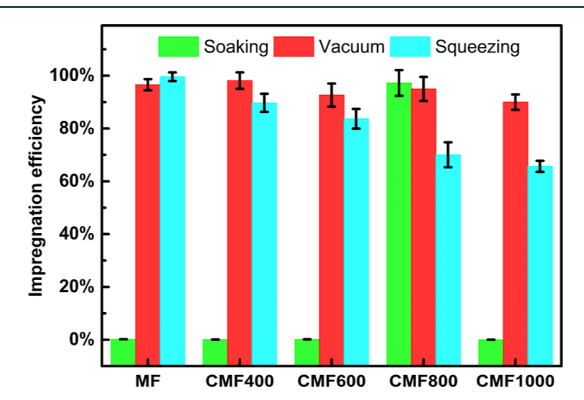


Figure 8. Impregnation efficiency of liquid $CaCl_2 \cdot 6H_2O$ in MF and CMFs using different impregnation methods.

efficiency by the vacuum method consistently exceeds 90% for all samples (Figure 8). This shows that the decreasing impregnation efficiency with increasing pyrolysis temperature observed for the squeezing impregnation is not due to the inherent surface properties of the CMFs. The discrepancy between the two impregnation methods can be explained by the decreasing elasticity of CMFs with an increasing degree of carbonization:²² the deformation required to expel all the trapped air becomes less reversible with increasing carbonation degree, which leads to decreased impregnation efficiency. To characterize the performance of the composite PCMs, each MF/CMF-CaCl₂·6H₂O composite was prepared by the most efficient impregnation method (e.g., soaking for SCMF800,

Energy & Fuels pubs.acs.org/EF Article

squeezing for SMF, and vacuum for SCMF400, SCMF600, and SCMF1000).

3.4. Effect of MF and CMF on the Thermal Energy Storage Performance of CaCl₂·6H₂O. *3.4.1.* Leakage. The leakage was measured by the weight loss of the form-stable MF/CMF-CaCl₂·6H₂O composites after keeping them at 30 °C for 1 h on the aluminum foil (Figure 9). The weight loss

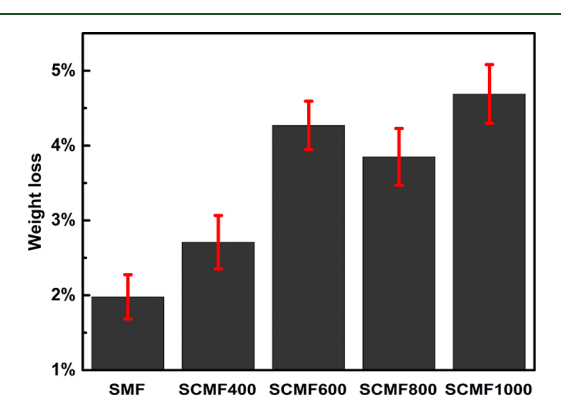


Figure 9. Weight loss of the molten $CaCl_2 \cdot 6H_2O/MF$ (CMFs) composites after keeping at 30 °C for 1 h on an aluminum foil.

corresponds to the trace amount of liquid $CaCl_2 \cdot 6H_2O$ left on the aluminum surface after the removal of the composite from the aluminum foil. The weight loss of all the samples is lower than 5 wt %, indicating an effective improvement of the form stability of liquid $CaCl_2 \cdot 6H_2O$. The SMF shows the least leakage of 2 wt % in this test.

3.4.2. Dehydration. TGA was used to characterize the dehydration of $CaCl_2 \cdot 6H_2O$ and its composites from room temperature to 60 °C under dry nitrogen (Figure 10). For all

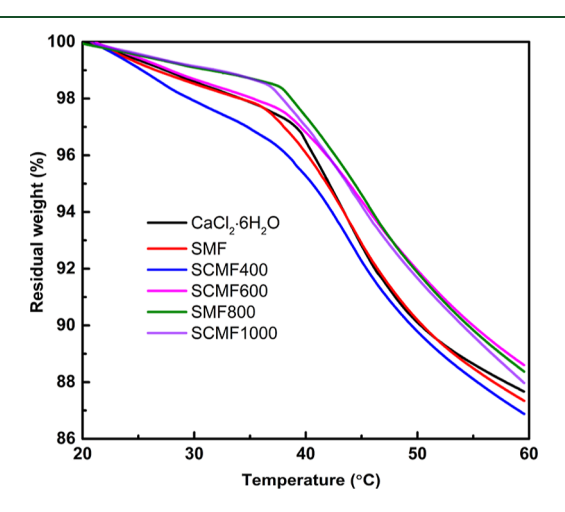


Figure 10. TGA of pure $CaCl_2 \cdot 6H_2O$ and $CaCl_2 \cdot 6H_2O$ -MF/CMF composites with 1 °C/min heating rate.

samples, dehydration starts with the onset of heating at a lower rate until \sim 37 °C, above which a much higher dehydration rate is observed. The least dehydration up to 37 °C is observed for SCMF800 and SCMF1000, corresponding to 1.48 wt % loss. In comparison, pure CaCl₂·6H₂O loses 2.49 wt % up to 37 °C. The SCMF600 shows the least dehydration of 11.4 wt % at 60 °C, with similar losses observed for SCMF800 and SCMF1000. The dehydration loss for pure CaCl₂·6H₂O at

60 °C is 12.3 wt %. This demonstrates the efficacy of encapsulation in suppressing dehydration.

3.4.3. Supercooling and Energy Density. The thermal energy density and phase-change temperatures were examined by DSC for pure CaCl₂·6H₂O and SMF (SCMFs) composites (Figure 11 and Table 1). The determination of the melting

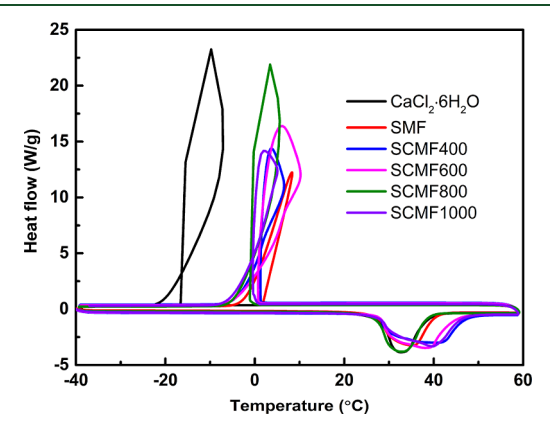


Figure 11. DSC curves of pure $CaCl_2 \cdot 6H_2O$ and $CaCl_2 \cdot 6H_2O/MF$ (CMFs) composites using 10 °C/min ramp rate between -40 °C and 60 °C.

Table 1. Melting Point $(T_{\rm m})$, Freezing Point $(T_{\rm c})$, Peak Temperature of Melting $(T_{\rm p})$, Enthalpy of Melting $(\triangle H_{\rm m})$ and Freezing $(\triangle H_{\rm c})$, and Thermal Energy Efficiency (f) of Pure CaCl₂·6H₂O and CaCl₂·6H₂O/MF(CMFs) Composites

samples	$\binom{T_{\mathrm{m}}}{(^{\circ}\mathrm{C})}$	$(^{\circ}C)$	<i>T</i> _c (°C)	$\frac{\Delta H_{\mathrm{m}}}{\left(\mathrm{J/g}\right)}$	$\frac{\Delta H_c}{(J/g)}$	f (%)
CaCl₂·6H₂O	28.1	32.7	-16.6	176.9	151.6	85.7
SMF	27.6	35.3	1.8	173.0	156.1	90.2
SCMF400	27.7	40.8	1.3	230.5	208.9	90.6
SCMF600	27.5	38.1	0.8	230.4	206.7	89.7
SCMF800	27.3	32.9	-1.1	180.2	162.8	90.3
SCMF1000	27.8	39.8	-0.4	229.8	206.2	89.7

point (T_m) , freezing point (T_c) , and peak temperature (T_p) is shown in Figure S10. The enthalpy of melting $(\Delta H_{\rm m})$ for pure CaCl₂·6H₂O is 176.9 J/g, which is consistent with ref 23. Similar values are also observed for SMF and SCMF800. However, the melting enthalpy observed for SCMF400, SCMF600, and SCMF1000 is substantially higher than that for CaCl₂·6H₂O. This is attributed to the dehydration of CaCl₂·6H₂O during vacuum impregnation, where an increase in melting enthalpy from 171 \pm 7 to 232 \pm 9 J/g has been reported when the crystal water content decreases from 51.09 to 49.35 wt %.46 The shift of T_p for SCMF400, SCMF600, and SCMF1000 is also consistent with the presence of a partially dehydrated phase that has an increased melting point (e.g., 44.3 °C for CaCl₂·4H₂O⁴⁷). The energy density of the produced carbon foam/CaCl₂·6H₂O composite PCM in this work is comparable with that of commercial Paraffin C18 and other common PCMs with a melting temperature between 25 °C and 30 °C (Figure S11).

A substantial difference in the cooling curve is observed between pure $CaCl_2 \cdot 6H_2O$ and the SMF/SCMF composites. The freezing point of the $CaCl_2 \cdot 6H_2O$ increases from -16.6 °C for pure $CaCl_2 \cdot 6H_2O$ to -1.1 to 1.8 °C for SMF and SCMFs, demonstrating the efficacy of encapsulation in the

suppression of supercooling. This suppressed supercooling increases the energy efficiency (f) by \sim 5% (Table 1).

3.4.4. Thermal Conductivity. Transient hot wire method was used to measure the thermal conductivity of CaCl₂·6H₂O and the SMF/SCMF composites in the liquid phase (Figure 12). The fitting of the measurement is shown in Figure S12.

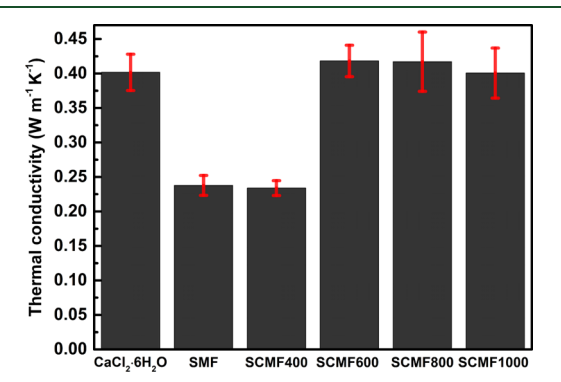


Figure 12. Thermal conductivity of pure $CaCl_2 \cdot 6H_2O$ (liquid) and molten $CaCl_2 \cdot 6H_2O \cdot MF/CMFs$ composites.

The measured thermal conductivity of $CaCl_2 \cdot 6H_2O$ is 0.40 \pm 0.03 W m⁻¹ K⁻¹, consistent with the reported values of 0.4~0.54 W m⁻¹ K⁻¹.

The thermal conductivities of the SCMF600, SCMF800, and SCMF1000 were measured to be 0.42 \pm 0.02, 0.42 \pm 0.04, and 0.40 \pm 0.04 W m $^{-1}$ K $^{-1}$, respectively, which are similar to that of liquid CaCl $_2$ ·6H $_2$ O. The low volume fraction (<1 vol %) open carbon foam network structure did not enhance the effective thermal conductivity of the composite. This is due to the matrices' amorphous nature, which lowers the carbon thermal conductivity. However, substantially smaller thermal conductivities are observed for SMF and SCMF400, which correspond to 0.24 \pm 0.02 and 0.23 \pm 0.01 W m $^{-1}$ K $^{-1}$, respectively.

Although substantial decreases in the thermal conductivity have been reported for the MF PCM, it is not clear from the literature what mechanism underlies this change given the low volume fraction of the foam in the composite (<1 vol %).⁴⁹ If intimate contact between the salt and the foam can be achieved everywhere in the composite, the thermal conductivity is expected to be governed by the thermal conductivity of the salt that occupies >99% volume of the composite. One plausible explanation for the reduced thermal conductivity measured for SMF and SCMF400 is the trapping of air bubbles in the composites, which leaves gaps along the path of heat conduction and greatly reduces the apparent thermal conductivity of the composite. Indeed, voids in the solid SMF composite are observed around the CaCl₂·6H₂O grains, especially near the sample surface where the hot wire probe is buried during the thermal conductivity measurement (Figures 13, S13, and Video S1).

3.5. Discussion. Thermal treatment of MF leads to transient surface deposits that modify the surface energy of the carbonized foam and hence hydrophilicity. In addition to the sodium carbonate phase identified as the surface deposits in a previous study,²² this work for the first time identifies a sodium cyanate phase in the surface deposits, which also facilitates the wettability with hydrated salt solutions. While other methods, such as surface oxidation^{50–52} and surfactant coating,^{25,53,54} have also been reported to directly modify the

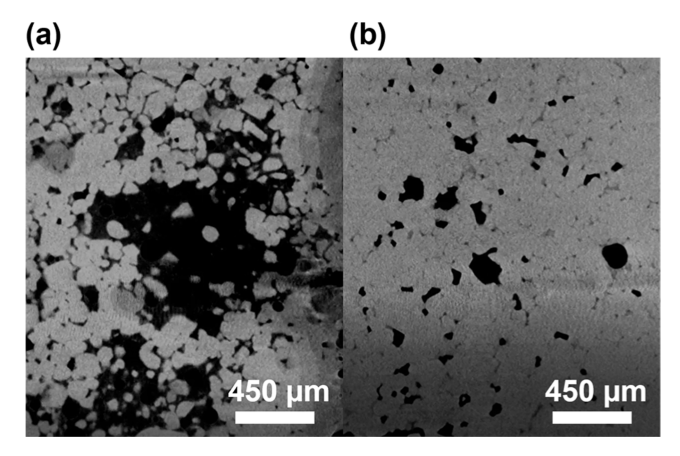


Figure 13. Virtual slices from the 3D X-ray CT images of the solid $CaCl_2 \cdot 6H_2O/MF$ composite (SMF) near (a) the surface and (b) the interior. Darker regions correspond to voids.

carbon surface, thermal treatment of MF provides a convenient one-step method to prepare hydrophilic carbon foams. Of the three impregnation methods employed in this work for preparing carbon/MF—salt hydrate composite PCMs, soaking impregnation is the most convenient method if the foam wets the salt hydrate. While vacuum impregnation, in general, shows high impregnation efficiency regardless of the wetting property of the foam, dehydration of the salt hydrates can occur, which changes the thermal properties of the salt hydrate. All MF and CMFs show a similar effect on the suppression of the supercooling of CaCl₂·6H₂O. Hence, the surface sodium deposits do not facilitate the nucleation of CaCl₂·6H₂O despite their marked effect on the surface energy of the CMF. The MF and CMFs reduce the supercooling of CaCl₂·6H₂O by 17 °C at a 10 °C/min ramp, which is superior to diatomite (11.4 °C at the same condition).²³

Despite the efficacy of the foam encapsulation method in suppressing the supercooling, adding a nucleating agent should be the most effective approach to decrease the supercooling of CaCl₂·6H₂O.⁵⁵ For example, 1 wt % BaCl₂ decreases the supercooling of CaCl₂·6H₂O by 32.7 °C at the same condition (Figure S14). Incorporation of a nucleating agent in MF and CMF is a promising strategy to decrease the supercooling of the inorganic salt hydrate PCM composites. Furthermore, coating the CaCl₂·6H₂O-MF/CMF composite with an impermeable layer, such as polyurethane, 49 will reduce or eliminate the weight loss while preserving the form stability of the PCM. In addition, graphitic carbon foam should be able to increase the thermal conductivity of the composite PCMs. 25,56 Finally, attention should be paid to the stoichiometry of salt hydrate PCM to optimize the energy storage density since a small change in the crystal water content of CaCl₂·6H₂O from 51.09 to 49.35 wt % can increase its energy density by more than 35%, 46 which is also observed in the present study.

4. CONCLUSIONS

The temperature and duration of the MF pyrolysis play an important role in the physical and chemical properties of the carbonized foam product. The formation of crystalline sodium carbonates and cyanates particles on the foam skeleton surface at 700–900 °C reduces the surface tension between the carbon foam and the inorganic molten salt, allowing the spontaneous impregnation of the carbon foam. The carbon foam-salt hydrate composite effectively suppresses supercooling and

dehydration and maintains the form stability with minimal salt leakage. This work demonstrates carbon foam as a promising host medium for preparing composite PCM using inorganic salt hydrate.

ASSOCIATED CONTENT

Solution Supporting Information

The Supporting Information is available free of charge at https://pubs.acs.org/doi/10.1021/acs.energyfuels.3c01275.

Photographic representation of the three impregnation methods to prepare salt hydrates composite; SEM images of the cross section of a skeleton of the MF, CMF400, CMF600, CMF800, CMF1000, and surface particles of the foams carbonized between 700 and 900 °C; the equation to calculate impregnation efficiency; open void space, skeleton density, and branch length of the MF, CMF400, CMF600, CMF800, and CMF1000; powder XRD patterns for CMF700, CMF800, CMF900, and Rietveld refined crystalline phases composition and content; FTIR spectrum for CMF700, CMF800, and CMF900; impregnation efficiency of CaCl₂·6H₂O in CMF700, CMF800, and CMF900 using soaking impregnation; impregnation efficiency of water in MF, CMF400, CMF600, CMF800, and CMF1000 using different impregnation methods; detailed DSC results for CaCl₂·6H₂O and its composites; melting enthalpy of different PCMs with a melting point between 25 and 30 °C; experimental data and fitting for the thermal conductivity measurement of the liquid CaCl₂·6H₂O and its composites; DSC result for CaCl₂·6H₂O with BaCl₂ as a nucleating agent; and the 3D X-ray CT images (PDF)

Voids in the solid SMF composite (AVI)

Voids in the solid SMF composite (AVI)

AUTHOR INFORMATION

Corresponding Author

Hao Liu – Materials Science and Engineering Program and Department of Chemistry, Binghamton University, Binghamton, New York 13902, United States; oorcid.org/0000-0003-0345-6647; Email: liuh@binghamton.edu

Authors

Yikang Jing — Materials Science and Engineering Program, Binghamton University, Binghamton, New York 13902, United States; © orcid.org/0009-0006-9729-2899

Kunal Dixit – Materials Science and Engineering Program, Binghamton University, Binghamton, New York 13902, United States

Scott N. Schiffres – Materials Science and Engineering Program and Department of Mechanical Engineering, Binghamton University, Binghamton, New York 13902, United States; orcid.org/0000-0003-1847-7715

Complete contact information is available at: https://pubs.acs.org/10.1021/acs.energyfuels.3c01275

Author Contributions

H.L. conceived and supervised the project. Y.J. worked on the synthesis and characterization of carbon foam and composites. K.D. conducted the thermal conductivity measurements with supervision from S.N.S. The manuscript was written through

contributions of all authors. All authors have given approval to the final version of the manuscript.

Notes

The authors declare no competing financial interest.

ACKNOWLEDGMENTS

H.L. and Y.J. acknowledge the funding support from the Integrated Electronics Engineering Center (IEEC) at Binghamton University. S.N.S. and K.D. acknowledge DoD grant 13000844-021 and NSF 1846157. The authors thank Dr. Anju Sharma for her assistance with the X-ray CT measurement.

ABBREVIATIONS

PCM = phase-change material

MF = melamine foam

CMF = carbonized melamine foam

SEM = scanning electron microscopy

FTIR = Fourier-transform infrared spectroscopy

XRD = powder X-ray diffraction

TGA = thermogravimetric analysis

DSC = differential scanning calorimetry

SMF = $CaCl_2 \cdot 6H_2O$ hydrated salt-melamine foam composite

 $SCMF = CaCl_2 \cdot 6H_2O$ hydrated salt-carbonized melamine foam composite

REFERENCES

- (1) Mofijur, M.; Mahlia, T. M. I.; Silitonga, A. S.; Ong, H. C.; Silakhori, M.; Hasan, M. H.; Putra, N.; Rahman, S. A. Phase change materials (PCM) for solar energy usages and storage: An overview. *Energies* **2019**, *12*, 3167.
- (2) Souayfane, F.; Fardoun, F.; Biwole, P.-H. Phase change materials (PCM) for cooling applications in buildings: A review. *Energy Build.* **2016**, *129*, 396–431.
- (3) Ling, Z.; Zhang, Z.; Shi, G.; Fang, X.; Wang, L.; Gao, X.; Fang, Y.; Xu, T.; Wang, S.; Liu, X. Review on thermal management systems using phase change materials for electronic components, Li-ion batteries and photovoltaic modules. *Renew. Sustain. Energy Rev.* **2014**, 31, 427–438.
- (4) Sharma, R.; Ganesan, P.; Tyagi, V.; Metselaar, H.; Sandaran, S. Developments in organic solid–liquid phase change materials and their applications in thermal energy storage. *Energy Convers. Manage.* **2015**, 95, 193–228.
- (5) Cabeza, L. F.; Castell, A.; Barreneche, C. d.; De Gracia, A.; Fernández, A. Materials used as PCM in thermal energy storage in buildings: A review. *Renew. Sustain. Energy Rev.* **2011**, *15*, 1675–1695.
- (6) Yu, K.; Liu, Y.; Yang, Y. Review on form-stable inorganic hydrated salt phase change materials: Preparation, characterization and effect on the thermophysical properties. *Appl. Energy* **2021**, *292*, 116845
- (7) Kenisarin, M.; Mahkamov, K. Salt hydrates as latent heat storage materials:Thermophysical properties and costs. *Sol. Energy Mater. Sol. Cells* **2016**, *145*, 255–286.
- (8) Beaupere, N.; Soupremanien, U.; Zalewski, L. Nucleation triggering methods in supercooled phase change materials (PCM), a review. *Thermochim. Acta* **2018**, *670*, 184–201.
- (9) Purohit, B.; Sistla, V. Inorganic salt hydrate for thermal energy storage application: A review. *Energy Storage* **2021**, *3*, No. e212.
- (10) Min, X.; Fang, M.; Huang, Z.; Liu, Y. g.; Huang, Y.; Wen, R.; Qian, T.; Wu, X. Enhanced thermal properties of novel shape-stabilized PEG composite phase change materials with radial mesoporous silica sphere for thermal energy storage. *Sci. Rep.* **2015**, *5*, 12964.
- (11) Zhao, Y.; Sun, B.; Du, P.; Min, X.; Huang, Z.; Liu, Y. g.; Wu, X.; Fang, M. Hierarchically channel-guided porous wood-derived shape-stabilized thermal regulated materials with enhanced thermal

- conductivity for thermal energy storage. Mater. Res. Express 2019, 6, 115515.
- (12) Cheng, F.; Zhang, X.; Wen, R.; Huang, Z.; Fang, M.; Liu, Y. g.; Wu, X.; Min, X. Thermal conductivity enhancement of form-stable tetradecanol/expanded perlite composite phase change materials by adding Cu powder and carbon fiber for thermal energy storage. *Appl. Therm. Eng.* **2019**, *156*, 653–659.
- (13) Li, X.; Zhao, Y.; Min, X.; Xiao, J.; Wu, X.; Mi, R.; Liu, Y. g.; Huang, Z.; Fang, M. Carbon nanotubes modified graphene hybrid Aerogel-based composite phase change materials for efficient thermal storage. *Energy Build.* **2022**, *273*, 112384.
- (14) Zahir, M. H.; Mohamed, S. A.; Saidur, R.; Al-Sulaiman, F. A. Supercooling of phase-change materials and the techniques used to mitigate the phenomenon. *Appl. Energy* **2019**, *240*, 793–817.
- (15) Wu, Y.; Wang, C.; Li, J.; Li, Y. Porous Hydroxyapatite Foams: Excellent Carrier of Hydrated Salt with Adjustable Pores for Thermal Energy Storage. *Ind. Eng. Chem. Res.* **2021**, *60*, 1259–1265.
- (16) Feng, W.; Qin, M.; Feng, Y. Toward highly thermally conductive all-carbon composites: Structure control. *Carbon* **2016**, 109, 575–597.
- (17) Giri, A.; Dionne, C. J.; Hopkins, P. E. Atomic coordination dictates vibrational characteristics and thermal conductivity in amorphous carbon. *npj Comput. Mater.* **2022**, *8*, 55.
- (18) Balandin, A. A. Thermal properties of graphene and nanostructured carbon materials. *Nat. Mater.* **2011**, *10*, 569–581.
- (19) Jing, J.-h.; Wu, H.-y.; Shao, Y.-w.; Qi, X.-d.; Yang, J.-h.; Wang, Y. Melamine foam-supported form-stable phase change materials with simultaneous thermal energy storage and shape memory properties for thermal management of electronic devices. *ACS Appl. Mater. Interfaces* **2019**, *11*, 19252–19259.
- (20) Du, Y.; Huang, H.; Hu, X.; Liu, S.; Sheng, X.; Li, X.; Lu, X.; Qu, J. Melamine foam/polyethylene glycol composite phase change material synergistically modified by polydopamine/MXene with enhanced solar-to-thermal conversion. *Renewable Energy* **2021**, *171*, 1–10.
- (21) Chen, W.; Liang, X.; Wang, S.; Gao, X.; Zhang, Z.; Fang, Y. Macro-encapsulated 3D phase change material: Na₂S₂O₃· SH₂O-NaOAc· 3H₂O/carbonized Melamine sponge composite as core and SiC modified polyurethane thin-layer as shell. *Compos. Sci. Technol.* **2021**, *214*, 108981.
- (22) Stolz, A.; Le Floch, S.; Reinert, L.; Ramos, S. M.; Tuaillon-Combes, J.; Soneda, Y.; Chaudet, P.; Baillis, D.; Blanchard, N.; Duclaux, L.; et al. Melamine-derived carbon sponges for oil-water separation. *Carbon* **2016**, *107*, 198–208.
- (23) Zhang, X.; Li, X.; Zhou, Y.; Hai, C.; Shen, Y.; Ren, X.; Zeng, J. Calcium chloride hexahydrate/diatomite/paraffin as composite shape-stabilized phase-change material for thermal energy storage. *Energy Fuels* **2018**, 32, 916–921.
- (24) Fu, L.; Wang, Q.; Ye, R.; Fang, X.; Zhang, Z. A calcium chloride hexahydrate/expanded perlite composite with good heat storage and insulation properties for building energy conservation. *Renewable Energy* **2017**, *114*, 733–743.
- (25) Duan, Z.-j.; Zhang, H.-z.; Sun, L.-x.; Cao, Z.; Xu, F.; Zou, Y.-j.; Chu, H.-l.; Qiu, S.-j.; Xiang, C.-l.; Zhou, H.-y. CaCl₂·6H₂O/Expanded graphite composite as form-stable phase change materials for thermal energy storage. *J. Therm. Anal. Calorim.* **2014**, *115*, 111–117.
- (26) Chen, S.; He, G.; Hu, H.; Jin, S.; Zhou, Y.; He, Y.; He, S.; Zhao, F.; Hou, H. Elastic carbon foam via direct carbonization of polymer foam for flexible electrodes and organic chemical absorption. *Energy Environ. Sci.* **2013**, *6*, 2435–2439.
- (27) Dullien, F. A. Porous Media: Fluid Transport and Pore Structure; Academic Press, 2012; Section 1, p 7.
- (28) Kang, C.; Park, Y.-H.; Van Lew, J. T.; Ying, A.; Abdou, M.; Cho, S. Transient hot-wire experimental system for measuring the effective thermal conductivity of a ceramic breeder pebble bed. *Fusion Sci. Technol.* **2017**, *72*, 1–8.
- (29) Bhattarai, B.; Pandey, A.; Drabold, D. Evolution of amorphous carbon across densities: An inferential study. *Carbon* **2018**, *131*, 168–174.

- (30) Savvatimskiy, A. Measurements of the melting point of graphite and the properties of liquid carbon (a review for 1963–2003). *Carbon* **2005**, 43, 1115–1142.
- (31) Dušek, M.; Chapuis, G.; Meyer, M.; Petricek, V. Sodium carbonate revisited. *Acta Crystallogr. Sect. B Struct. Sci.* **2003**, *59*, 337–352.
- (32) Wu, K.; Brown, I. A neutron diffraction study of Na₂CO₃•H₂O. *Acta Crystallogr. Sect. B Struct. Crystallogr. Cryst. Chem.* **1975**, 31, 890−892.
- (33) Bassiere, M. The Structure of Sodium Isocyanate. C.r.hebd.-Seanc.Acad.Sci. 1938, 206, 1309-1311.
- (34) Reckeweg, O.; Schulz, A.; Leonard, B.; DiSalvo, F. J. Single-Crystal X-Ray Diffraction Study of Na[OCN] at 170 K and its Vibrational Spectra. Z. Naturforsch. B Chem. Sci. 2010, 65, 528–532.
- (35) Ter, H. W. P. Process of making sodium cyanate. U.S. Patent 2,690,956 A, 1954.
- (36) Li, X.; Zhang, J.; Shen, L.; Ma, Y.; Lei, W.; Cui, Q.; Zou, G. Preparation and characterization of graphitic carbon nitride through pyrolysis of melamine. *Appl. Phys. A* **2009**, *94*, 387–392.
- (37) Pham, V. H.; Dickerson, J. H. Superhydrophobic silanized melamine sponges as high efficiency oil absorbent materials. *ACS Appl. Mater. Interfaces* **2014**, *6*, 14181–14188.
- (38) Wu, X.; Tao, Y.; Lu, Y.; Dong, L.; Hu, Z. High-pressure pyrolysis of melamine route to nitrogen-doped conical hollow and bamboo-like carbon nanotubes. *Diamond and related materials* **2006**, 15, 164–170.
- (39) Merline, D. J.; Vukusic, S.; Abdala, A. A. Melamine formaldehyde: curing studies and reaction mechanism. *Polym. J.* **2013**, *45*, 413–419.
- (40) Hadži, D.; Škrbljak, M. 158. Infrared absorption bands associated with the NH group. Part I. Some secondary aromatic amines. *J. Chem. Soc.* **1957**, *0*, 843–847.
- (41) Trends, S. G. Gas Phase Infrared Spectrum of Formaldehyde, H2C= O. Accessed July 21, 2023.
- (42) Mircescu, N. E.; Oltean, M.; Chiş, V.; Leopold, N. FTIR, FT-Raman, SERS and DFT study on melamine. *Vib. Spectrosc.* **2012**, *62*, 165–171.
- (43) Waddington, T. 499. Lattice parameters and infrared spectra of some inorganic cyanates. *J. Chem. Soc.* **1959**, 2499–2502.
- (44) Brooker, M. H.; Bates, J. B. Raman and Infrared Spectral Studies of Anhydrous Li₂CO₃ and Na₂CO₃. *J. Chem. Phys.* **1971**, *54*, 4788–4796.
- (45) Al-Zaidi, E.; Fan, X. Effect of aqueous electrolyte concentration and valency on contact angle on flat glass surfaces and inside capillary glass tubes. *Colloids Surf., A* **2018**, *543*, 1–8.
- (46) Schmit, H.; Rudaleviciene, D.; Rathgeber, C.; Hiebler, S. Calorimetric Investigation of Two Factors Influencing the Maximum Storage Capacity of Calcium Chloride Hexahydrate. *IOP Conf. Ser. Mater. Sci. Eng.* **2019**, *660*, 012076.
- (47) Ushak, S.; Suárez, M.; Véliz, S.; Fernández, A. G.; Flores, E.; Galleguillos, H. R. Characterization of calcium chloride tetrahydrate as a phase change material and thermodynamic analysis of the results. *Renewable Energy* **2016**, *95*, 213–224.
- (48) Sutjahja, I.; Silalahi, A.; Wonorahardjo, S.; Kurnia, D. Thermal conductivity of phase-change material CaCl₂·6H₂O with ZnO nanoparticle dopant based on temperature-history method. *Rev. Rom. Mater.* **2019**, 49, 185–192.
- (49) Chen, W.; Liang, X.; Wang, S.; Gao, X.; Zhang, Z.; Fang, Y. Polyurethane macro-encapsulation for CH₃COONa·3H₂O-Na₂S₂O₃· 5H₂O/Melamine sponge to fabricate form-stable composite phase change material. *Chem. Eng. J.* **2021**, *410*, 128308.
- (50) Zhou, J.-H.; Sui, Z.-J.; Zhu, J.; Li, P.; Chen, D.; Dai, Y.-C.; Yuan, W.-K. Characterization of surface oxygen complexes on carbon nanofibers by TPD, XPS and FT-IR. *Carbon* **2007**, *45*, 785–796.
- (51) Rosca, I. D.; Watari, F.; Uo, M.; Akasaka, T. Oxidation of multiwalled carbon nanotubes by nitric acid. *Carbon* **2005**, *43*, 3124–3131.

- (52) Yoon, C.-M.; Long, D.; Jang, S.-M.; Qiao, W.; Ling, L.; Miyawaki, J.; Rhee, C.-K.; Mochida, I.; Yoon, S.-H. Electrochemical surface oxidation of carbon nanofibers. *Carbon* **2011**, *49*, 96–105.
- (53) Zhou, Y.; Sun, W.; Ling, Z.; Fang, X.; Zhang, Z. Hydrophilic Modification of Expanded Graphite to Prepare a High-Performance Composite Phase Change Block Containing a Hydrate Salt. *Ind. Eng. Chem. Res.* **2017**, *56*, 14799–14806.
- (54) Zhang, Y.; Sun, J.; Ma, G.; Wang, Z.; Xie, S.; Jing, Y.; Jia, Y. Hydrophilic expanded graphite-magnesium nitrate hexahydrate composite phase change materials: Understanding the effect of hydrophilic modification on thermophysical properties. *Int. J. Energy Res.* 2019, 43, 1121–1132.
- (55) Lane, G. A. Phase change materials for energy storage nucleation to prevent supercooling. *Sol. Energy Mater. Sol. Cells* **1992**, *27*, 135–160.
- (56) Zhao, Y.; Min, X.; Huang, Z.; Liu, Y. g.; Wu, X.; Fang, M. Honeycomb-like structured biological porous carbon encapsulating PEG: A shape-stable phase change material with enhanced thermal conductivity for thermal energy storage. *Energy Build.* **2018**, *158*, 1049–1062.